Computation

CrossMark

Correlation between three-dimensional and cross-sectional characteristics of ideal grain growth: large-scale phase-field simulation study

Eisuke Miyoshi[1], Tomohiro Takaki[2,*], Munekazu Ohno[3], Yasushi Shibuta[4], Shinji Sakane[1], Takashi Shimokawabe[5], and Takayuki Aoki[6]

[1] Graduate School of Science and Technology, Kyoto Institute of Technology, Matsugasaki, Sakyo-ku, Kyoto 606-8585, Japan
[2] Faculty of Mechanical Engineering, Kyoto Institute of Technology, Matsugasaki, Sakyo-ku, Kyoto 606-8585, Japan
[3] Division of Materials Science and Engineering, Faculty of Engineering, Hokkaido University, Kita 13 Nishi 8, Kita-ku, Sapporo, Hokkaido 060-8628, Japan
[4] Department of Materials Engineering, The University of Tokyo, 7-3-1 Hongo, Bunkyo-ku, Tokyo 113-8656, Japan
[5] The Supercomputing Division, Information Technology Center, The University of Tokyo, 2-11-16 Yayoi, Bunkyo-ku, Tokyo 113-8658, Japan
[6] Global Scientific Information and Computing Center, Tokyo Institute of Technology, 2-12-1 I7-3 O-okayama, Meguro-ku, Tokyo 152-8550, Japan

ABSTRACT

Grain growth is one of the most fundamental phenomena affecting the microstructure of polycrystalline materials. In experimental studies, three-dimensional (3D) grain growth is usually investigated by examining two-dimensional (2D) cross sections. However, the extent to which the 3D microstructural characteristics can be obtained from cross-sectional observations remains unclear. Additionally, there is some disagreement as to whether a cross-sectional view of 3D grain growth can be fully approximated by 2D growth. In this study, by employing the multi-phase-field method and parallel graphics processing unit computing on a supercomputer, we perform large-scale simulations of 3D and 2D ideal grain growth with approximately three million initial grains. This computational scale supports the detailed comparison of 3D, cross-sectional, and 2D grain structures with good statistical reliability. Our simulations reveal that grain growth behavior in a cross section is very different from those in 3D and fully 2D spaces, in terms of the average and distribution of the grain sizes, as well as the growth kinetics of individual grains. On the other hand, we find that the average grain size in 3D can be estimated as being around 1.2 times that observed in a cross section, which is in good agreement with classical theory in the stereology. Furthermore, based on the Saltykov–Schwartz method, we propose a predictive model that can estimate the 3D grain size distribution from the cross-sectional size distribution.

Address correspondence to E-mail: takaki@kit.ac.jp

Springer

Introduction

During the heat treatment of a polycrystalline material, microstructural evolution takes place through the competitive growth of grains due to the curvature-driven boundary migrations. This metallurgical phenomenon, i.e., grain growth, is of great importance to the development of superior materials, since the physical properties of polycrystals largely depend on the average and distribution of their grain sizes [1–3]. Thus, intensive studies have been undertaken to better understand and predict grain growth.

To experimentally observe grain growth, three-dimensional (3D) samples are usually investigated by examining their two-dimensional (2D) cross sections. However, the extent to which the 3D microstructural characteristics can be obtained from the cross sections is not clear. In the area of stereology [4], many efforts have been devoted to the analytical extraction of 3D microstructural information from cross-sectional observations. Meanwhile, some experimental studies have undertaken direct measurements of 3D grain growth using 3D characterization techniques, such as grain separating [5–7], serial sectioning [8–11], and X-ray microtomography [12, 13]. One of the most detailed investigations in this area was reported by Rhines et al. [8], who undertook very laborious experiments to measure and compare the temporal variations in 3D and cross-sectional grain structures. Significant discrepancies between the results for each dimension led them to conclude that 3D microstructures and their evolution kinetics cannot be inferred from cross sections, and instead must be determined in 3D space. On the validity or universality of this conclusion, several researchers have raised questions [1, 2, 14–16], suggesting that the annealing time used by Rhines et al. [8] may not have been long enough to remove the initial anisotropy present in the mechanically processed specimens. Currently, however, the theory remains controversial due to issues with the associated experiments, specifically the enormous amounts of labor required for the temporal observation of 3D microstructures, the challenges associated with maintaining the desired specimen conditions, and the issue of sampling bias arising from the limited analysis volume and spatial resolution [17].

Numerical simulation provides a helpful means of addressing the above issues, because it enables us to easily compare grain growth in 3D and its cross sections for arbitrarily controlled systems. In this regard, several numerical studies have been conducted using continuum-based grain growth models, such as the Monte Carlo model [18–20], vertex or front-tracking model [21–24], surface-evolver model [25], and phase-field model [26]. However, even for the simplest (or 'ideal') grain growth with isotropic grain boundary properties, a conclusive consensus has yet to be established. For instance, grain size distributions during the steady-state regime, in which the normalized size distribution is time-invariant, appearing in the literature exhibit large discrepancies; this is true for both 3D and cross-sectional size distributions. Moreover, while the Monte Carlo study by Anderson et al. [18] reported that cross sections through an evolving 3D grain structure can be well approximated by a fully 2D simulation, the vertex simulations conducted by Weygand et al. [23] showed clear dissimilarities between the cross-sectional and 2D grain growth. These discrepancies could be attributed to the limitations of the previous simulations [27], namely large noise and lattice anisotropy in the Monte Carlo simulations, grain coalescence caused by a limited number of grain orientations, and a statistically insufficient number of grains in the computational system, all of which prevent reliable grain growth statistics from being obtained.

In recent years, there has been great progress in grain growth simulation using the phase-field model: the multi-phase-field (MPF) models developed in several works [28–33] and the active parameter tracking (APT) algorithm adopted by three research groups [27, 34, 35] allowed for the accurate and effective computation of grain growth while avoiding the artificial coalescence of grains. In particular, the MPF model reported by Steinbach et al. [28, 31] exhibits quite a high degree of computational efficiency, since the grain boundary region is clearly defined by using the double-obstacle potential and, thus, the governing equation does not have to be solved outside of the boundary region. Furthermore, rapid developments in high-performance computing have been such that it is now easy to perform large-scale phase-field simulations. Some groups conducted phase-field grain growth simulations with several tens of thousands of grains by employing parallel-computing techniques [36–39]. Graphics processing units (GPUs), which were originally

developed to effectively handle graphical output, have also proven to be extremely useful for handling computations on a greatly enlarged scale and have been successfully applied to computational materials science [40–45]. In our previous studies, by enabling massive parallel GPU computing on the GPU-rich supercomputer TSUBAME at the Tokyo Institute of Technology, it proved possible to achieve large-scale phase-field simulations of various solidification processes [46–51]. Recently, we applied a parallel GPU computing scheme to the MPF model of Steinbach and Pezzolla [31] and succeeded in simulating 3D ideal grain growth for large-scale polycrystalline systems with 2560^3 grid points and more than three million initial grains [52]. This computational scale enabled us to observe true steady-state growth with a statistically sufficient number of grains and to elucidate the statistical behaviors of the phenomenon.

In the present study, by focusing on ideal grain growth, we set out to elucidate the correlation between 3D and cross-sectional microstructures via large-scale phase-field simulations. We also wanted to address the question of whether the cross-sectional view of 3D grain growth can be fully approximated by 2D growth. The remainder of this paper is laid out as follows: first, "Simulation methodology" section describes the methodology of the grain growth simulations. Next, based on the simulated data, "Results and discussion" section examines grain growth in the 3D, cross-sectional, and 2D domains. The behaviors of the systems and individual grains with different dimensionalities are compared in detail from both morphological and kinetic viewpoints. Finally, in the same section, we discuss an analytical means of estimating the 3D grain structures from cross-sectional observations.

Simulation methodology

Multi-phase-field model

The MPF model proposed by Steinbach and Pezzolla [31] is employed for simulating the ideal grain growth. This model represents a polycrystalline system including N grains through N phase-field variables ϕ_i ($i = 1, 2,..., N$), which take a value of 1 in the ith grain and 0 in the other grains, smoothly changing from 1 to 0 at the grain boundaries. The sum of the phase fields at any spatial point in the system must be conserved as:

$$\sum_{i=1}^{N} \phi_i = 1. \tag{1}$$

For ideal grain growth without additional driving forces other than the grain boundary energy, the total free energy of the system, F, can be expressed as:

$$F = \int_V \sum_{i=1}^{N} \sum_{j=i+1}^{N} \left(-\frac{a_{ij}^2}{2} \nabla\phi_i \cdot \nabla\phi_j + W_{ij}\phi_i\phi_j \right) \, dV, \tag{2}$$

where a_{ij} and W_{ij} are the gradient coefficient and barrier height of the boundary between the ith and jth grains, respectively. The time-evolution equation of the phase field ϕ_i satisfying Eq. (1) is given for each spatial point by:

$$\frac{\partial\phi_i}{\partial t} = -\frac{2}{n} \sum_{j=1}^{N} s_i s_j M_{ij}^{\phi} \left(\frac{\delta F}{\delta\phi_i} - \frac{\delta F}{\delta\phi_j} \right), \tag{3}$$

where n is the number of nonzero phase fields at the point; s_i is a step function that takes a value of 1 if $\phi_i > 0$ and otherwise vanishes; and M_{ij}^{ϕ} is the phase-field mobility of the boundary between the ith and jth grains. The functional derivative of F [Eq. (2)] can be calculated as:

$$\frac{\delta F}{\delta\phi_i} = \sum_{k=1}^{N} \left(\frac{a_{ik}^2}{2} \nabla^2\phi_k + W_{ik}\phi_k \right). \tag{4}$$

Finally, the time-evolution equation reduces to:

$$\frac{\partial\phi_i}{\partial t} = -\frac{2}{n} \sum_{j=1}^{N} s_i s_j M_{ij}^{\phi}$$
$$\times \sum_{k=1}^{N} \left\{ \frac{1}{2} \left(a_{ik}^2 - a_{jk}^2 \right) \nabla^2\phi_k + \left(W_{ik} - W_{jk} \right)\phi_k \right\}. \tag{5}$$

M_{ij}^{ϕ}, a_{ij}, and W_{ij} are related to the width (δ), energy (σ_{ij}), and mobility (M_{ij}) of the grain boundary according to the following equations:

$$M_{ij}^{\phi} = \frac{\pi^2}{8\delta} M_{ij}, \quad a_{ij} = \frac{2}{\pi}\sqrt{2\delta\sigma_{ij}}, \quad W_{ij} = \frac{4\sigma_{ij}}{\delta}. \tag{6}$$

Note that, for accurately performing phase-field simulations, a sufficient number of grid points must be contained within the boundary width δ to resolve the boundary regions. If necessary, δ can be set so as to reproduce a realistic grain boundary width

($\sim$ nm) by using fine numerical grids [53]. In the current simulations, however, δ is treated as an artificial quantity and used only to implicitly track the grain boundary positions by the regions where non-zero phase fields coexist. Here, we set δ to six times the grid spacing, which has been reported to be a good compromise between computational accuracy and cost [27].

Computational conditions

To elucidate the similarities or dissimilarities between 3D, cross-sectional, and 2D ideal grain growth, we performed both 3D and 2D simulations. Figure 1a, c shows the computational systems employed for simulating 3D and 2D ideal grain growth, which consist of 3125000 and 3000000 initial grains, respectively, under periodic boundary conditions. Here, the grains are distinguished according to their colors. The cross sections perpendicular to each axis of the 3D system contain an average of approximately 26000 grains per section. An example of the sections (at the center of the z axis) is shown in Fig. 1b. Using square or cubic regular grids, the domains were divided into $2560 \times 2560 \times 2560$ grid points for the 3D system and into 32000×32000 grid points for the 2D system. The time increments (Δt_{3D} for the 3D system and Δt_{2D} for the 2D system), grid spacing (Δx), grain boundary energy (σ), and mobility (M) were set as follows, being non-dimensionalized with typical scales of 1 s, 10^{-6} m, 1 J m^{-2}, and 10^{-12} m^4 J^{-1} s^{-1}, respectively: $\Delta t_{3D} = 0.075$, $\Delta t_{2D} = 0.1125$, $\Delta x = 1$, $\sigma = 1$, and $M = 1$. To guarantee the statistical reliability of the results, three replicated

simulations with different initial structures were performed for both the 3D and 2D cases. For each simulation run, the initial grain structures, of a random shape, were created by growing randomly distributed nuclei using a constant driving force. Here, note that the numerical accuracy of phase-field grain growth simulation is generally determined by the relative grain size compared to the grain boundary width δ, in addition to the grid resolution of grain boundaries (i.e., the number of grids contained within δ) [27]. In the current MPF simulations, δ was set to $6\Delta x$ for both the 2D and 3D systems; further, the ratio of the initial average grain radius, $\langle R(0) \rangle$, to δ was almost same ($\langle R(0) \rangle / \delta \approx 1.7$) in both the cases. Therefore, the comparison of the 2D and 3D simulations is fair. We also note that although the above computational conditions for the 3D system were basically same as those used in our previous study [52], some new simulations were performed as part of the present study to analyze the cross-sectional microstructures in detail. The initial structures for the present simulations differ from those used in the previous study [52].

To perform the large-scale simulations, we utilized our own CUDA C code [52] that was specifically developed for parallel GPU computation. The code decomposes an entire computational domain into small subdomains, each of which is assigned to one GPU. The connection of the boundary data of the GPUs is performed via their host CPUs [46], while the internode communication is implemented using the message-passing interface (MPI). To reduce the memory requirements, the APT algorithm [27, 34, 35]
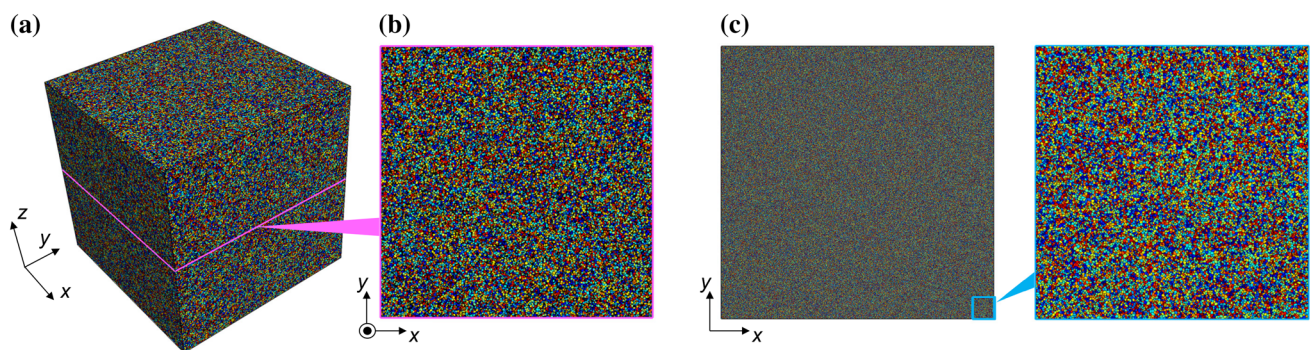

Figure 1 Polycrystalline systems used for simulating 3D and 2D ideal grain growth. **a** 3D system with $2560 \times 2560 \times 2560$ grid points and 3125000 initial grains. **b** Cross-sectional plane of (**a**) at the center of the z axis. **c** 2D system with 32000×32000 grid points and 3000000 initial grains. The light panel in (**c**) shows the overall computational domain, while the right one displays part (2560×2560 points) of the overall domain indicated by the blue frame. In all the panels, grains are distinguished by different colors.

proposed by Kim et al. [27] is used, storing only nonzero phase-field variables; the maximum number of stored variables at each grid point is set to seven. All computations were carried out on the GPU-rich supercomputer TSUBAME at the Tokyo Institute of Technology, using 200 GPUs (NVIDIA Tesla P100) for the 3D simulations and 64 GPUs (NVIDIA Tesla K20X) for the 2D simulations.

Results and discussion

Using the above-mentioned computational conditions, we performed 3D simulations for a period of $75000\Delta t_{3D}$ (i.e., 5625 in dimensionless time), after which around 20000 grains remained in each system. The required computation time per simulation was about 1 day. The 2D simulations were performed over a longer duration of $200000\Delta t_{2D} = 22500$, since the progress of the 2D grain growth is much slower than that of the 3D growth. After the simulations, roughly 40000 grains remained in each system.

Figure 2 depicts the evolved microstructures obtained for the 3D, cross-sectional, and 2D domains after the simulations, starting from the initial structures shown in Fig. 1. For reference, movies of the evolution processes are provided in the Supplementary Material. In all the panels of Fig. 2, we can see that the grains generally exhibit equi-axed shapes, as would be expected for microstructures formed through ideal grain growth. Below, we present a detailed analysis and discussion of the grain growth with different dimensionalities based on the simulated data. Note that, hereafter, the radius R of a 3D grain, R_{3D}, is defined as its volume (V)-equivalent radius, $\sqrt[3]{3V/(4\pi)}$; those of a cross-sectional grain, R_{3DX}, and 2D grain, R_{2D}, are determined from their area (A)-equivalent radius, $\sqrt{A/\pi}$.

Determining the grain characteristics

To analyze the microstructures obtained from phase-field simulations, two different methods have been used, namely simple summation [27] and cluster enumeration [54]. In the simple summation, the volume V_i (or area A_i for 2D) of a given grain i is calculated by simply integrating the corresponding phase field ϕ_i:

$$V_i = \int_V \phi_i \, \mathrm{d}V. \tag{7}$$

On the other hand, the cluster enumeration evaluates the V_i value based on the binarization processing:

$$V_i = \int_V O_i \, \mathrm{d}V, \tag{8}$$

where $O_i(\mathbf{r})$ is an operator that takes a value of 1 if ϕ_i has the largest value of all the phase fields at a spatial point $\mathbf{r}$. Otherwise, it vanishes.

Herein, to test the applicability of the above methods to the analysis of 3D, cross-sectional, and 2D grain structures, we calculated the grain size distributions of the simulated microstructures shown in Fig. 2 using both methods. The results are shown in Fig. 3, as normalized grain size histograms ($R/\langle R \rangle$, where $\langle R \rangle$ denotes the average grain radius) which were built using a typical bin width (0.1). In the analysis of the cross-sectional grain structure, we took 20 evenly spaced planes along each coordinate axis (i.e., 60 planes in total) and sampled all the grains appearing on those planes. The same is
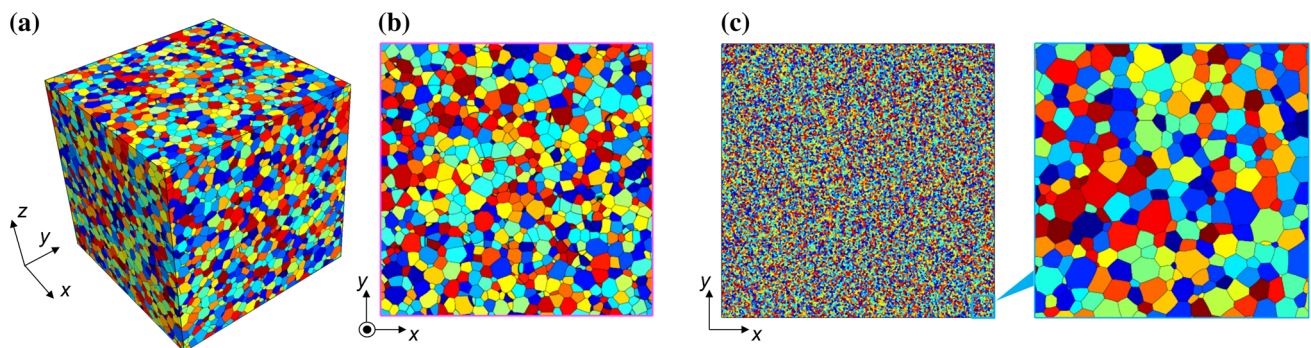

Figure 2 Evolved microstructures in 3D and 2D ideal grain growth simulations starting from the initial structures shown in Fig. 1. **a** 3D microstructure at $t = 75000\Delta t_{3D}$. **b** Cross-sectional plane at the center of the z axis. **c** 2D microstructure at $t = 200000\Delta t_{2D}$.
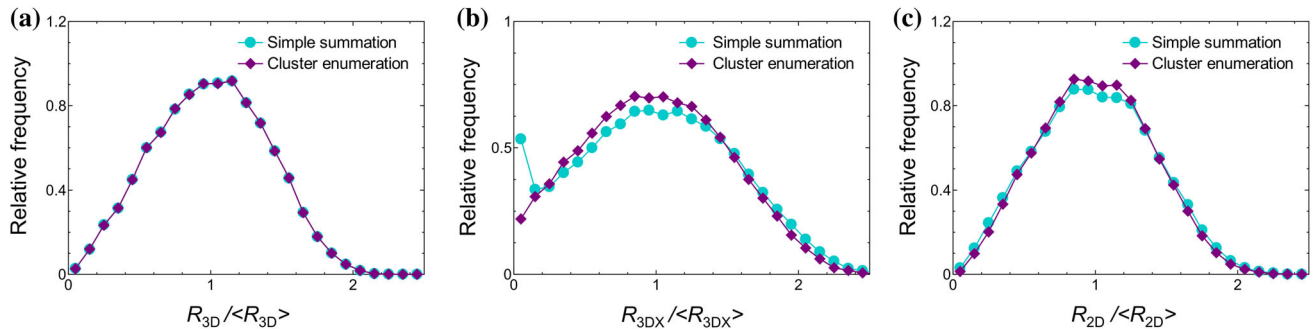
Figure 3 Grain size distributions obtained for microstructures shown in Fig. 2 using simple summation and cluster enumeration. **a** 3D grains. **b** Cross sections of 3D grains. **c** 2D grains. In the analysis of the cross-sectional grain size distributions, a total of 60 evenly spaced planes are taken and all grains appearing on the planes are sampled.

assumed in the remainder of this paper. Figure 3a shows that the simple summation and cluster enumeration give almost the same results for the evaluation of the 3D grain size distribution. Therefore, both methods are regarded as being valid for this application. In Fig. 3c, we can see slight differences between the analyzed 2D size distributions, in terms of their broadness and peak height. However, the shapes of the distributions are similar, with the difference in the peak heights being minimal (around 5%). In contrast, as shown in Fig. 3b, the results obtained for the cross sections exhibit significant differences: while the grain size distribution obtained from the cluster enumeration produces a smooth curve, that from the simple summation suddenly jumps at the smallest grain size class. This sudden jump is probably a result of the diffuse nature of the phase-field model. That is, when the binarization processing is not applied, a large amount of very small grains, cut near the edges of the diffuse interfaces, can appear in the cross sections. Indeed, a jump in the cross-sectional grain size distribution is not observed in the results obtained with the sharp interface models, including the vertex and front-tracking models [22–24].

Based on these results, for the analysis of cross-sectional microstructures described below, we mainly used cluster enumeration; simple summation was used only to calculate the time derivative of the individual grain sizes (dR/dt) in Figs. 7 and 8. On the other hand, the 3D and 2D microstructures were analyzed by simple summation, in the same way as in our previous studies [52, 55].

Statistical aspects of grain growth

This section investigates the statistical behaviors of ideal grain growth with different dimensionalities. First, Fig. 4 shows the temporal variations in the grain size distribution for the 3D, cross-sectional, and 2D domains. The numerical data points are given as the average of three replicated simulations with error bars representing the standard deviation, which is the same in the following figures. Most of the error bars are smaller than the symbols, confirming a high degree of statistical reliability of the results. In Fig. 4, we can see that all the grain size distributions rapidly become broader in the early stages of grain growth. During the later stages, however, the changes in the grain size distribution are rather small. In particular, in the period of $t \geq 35000\Delta t_{3D}$ for 3D and the cross sections and that of $t \geq 100000\Delta t_{2D}$ for 2D, almost no changes are observed, while the statistical errors are very small, indicating that the systems have reached their steady states. If, in Fig. 4, we compare (a) and (c), we find that the 3D and 2D steady-state size distributions exhibit a similar tendency in terms of their peak height and position, as well as their symmetry. A visible difference between the 2D steady-state size distribution and that of the 3D is the existence of a plateau around the peak in the 2D case, which is consistent with previously reported results [23, 24, 27]. In Fig. 4b, the steady-state shape of the cross-sectional grain size distribution exhibits characteristics that are quite different from those of the 3D and full 2D size distributions, in that it has a lower peak height and right-skewed shape.

Here, we should note the Monte Carlo study of ideal grain growth performed by Song et al. [19]; they reported that the transient time required to reach the
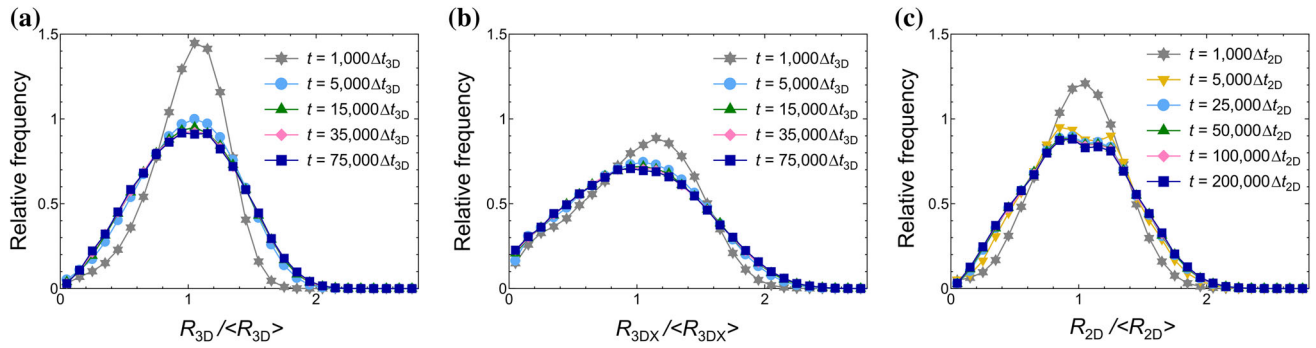
Figure 4 Temporal variations in grain size distribution for **a** 3D grains, **b** cross sections of 3D grains, and **c** 2D grains. Numeric data points are given as the average of three replicated simulations, with error bars representing the standard deviation. Most of the error bars are smaller than the symbols.

steady state is much longer in 3D than in the cross sections and, thus, the achievement of the steady state in 3D cannot be inferred from cross-sectional observations. In our simulations, however, there is no significant difference in the duration of the transient time in the 3D and cross-sectional growth (around $35000\Delta t_{3D}$ in both cases). This discrepancy is probably a consequence of the computational scale that we employed (a grain number that is 750 times greater than that used by Song et al. [19]), as well as the large amount of noise in the Monte Carlo simulation. Provided the initial grain structure is fully homogeneous, and the analyzed data are free of statistical bias, we believe that the achievement of the steady state in 3D ideal grain growth can be judged from the cross sections.

Further, it is worth mentioning that the symmetric grain size distribution obtained from our 2D MPF simulations, though consistent with other continuum-based simulation results [23, 24, 27], is largely different from the lognormal-like distribution observed in 2D atomistic simulations [56] and experiments for thin metal films [57]. One of the possible sources of this deviation is miscounting of the grains in atomistic simulations and experiments, which is inevitable due to the difficulty in detecting low-angle grain boundaries [58–60]. Another possible source is some grain growth-related factor not considered in the current simulations for the ideal grain growth. For example, previous grain growth simulations [54, 55, 61–63] demonstrated that grain rotation [61, 62], anisotropic boundary properties [54, 55, 62], and triple junction drag [63] can cause the asymmetry in grain size distribution. In addition, although the conventional MPF models including

that employed here can accurately handle the ideal grain growth [27, 30, 64], Tóth et al. [65] pointed out that these models do not fully satisfy the criteria for mathematical and physical consistency. They also simulated 2D grain growth using a fully consistent MPF model [65] and observed more asymmetric grain size distributions compared to those predicted by other MPF models. Further investigation of the origins of the contradictory results will be addressed elsewhere.

Next, we examined the kinetics of the systems. Figure 5 shows the temporal variations in the squared average grain size ($\langle R \rangle^2$) for each dimension, with all error bars being smaller than 0.2% of the mean. Fitted curves for the plots were calculated and are depicted in the figure using the well-known parabolic law of steady-state grain growth [66, 67]:

$$\langle R(t) \rangle^2 - \langle R(t_0) \rangle^2 = KM\sigma(t - t_0), \qquad (9)$$

where t_0 is an initial time and K is the kinetic coefficient. The K values are obtained as 0.478, 0.334, and 0.282 for 3D, the cross sections, and 2D, respectively, by applying the least-square fitting to the steady-state regimes ($t \geq 35000\Delta t_{3D}$ in 3D and the cross sections; $t \geq 100000\Delta t_{2D}$ in 2D). Figure 5 reveals that $\langle R \rangle^2$ increases linearly with time in accordance with the parabolic law in all cases. However, the obtained values of K differ greatly in each case, showing that the grain growth in 3D proceeds most rapidly with $K = 0.478$, followed by those in the cross sections ($K = 0.334$) and 2D ($K = 0.282$).

The above results allow us to conclude that the size distribution and evolution kinetics of the cross-sectional grains are clearly different from those of fully 2D grains. Furthermore, compared to the 3D space, a higher fraction of relatively small grains and a
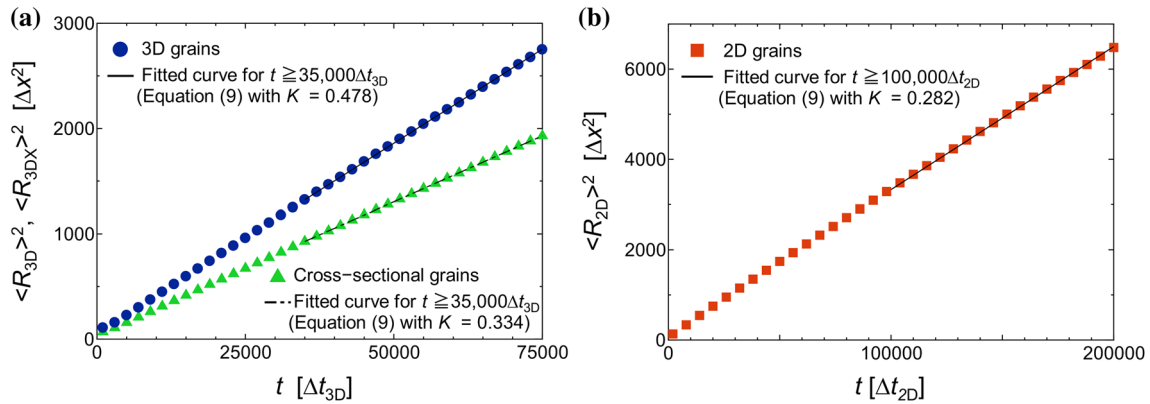
Figure 5 Temporal variations in average grain size for **a** 3D and cross-sectional grains and **b** 2D grains. In both panels, numeric data points are given as the average of three replicated simulations. Error bars (standard deviations) are all smaller than the symbols.

smaller average size are observed for the cross sections. This difference between the 3D and cross-sectional microstructures probably arises from the fact that the 3D grains can be cut such that they are apparently smaller than their true 3D sizes (i.e., stereological effect [4]). This can be confirmed in Fig. 6, in which we plot the relationship between the cross-sectional and 3D grain sizes in the steady-state regime (at $t = 75000\Delta t_{3D}$). The black diamonds indicate the average 3D grain sizes for each cross-sectional size class obtained by averaging three replicated simulations. The light-gray circles indicate the data for individual grains, with 5000 randomly sampled grains from the three simulations being plotted to better visualize the density of the data points. In Fig. 6, we can see that most of the grains have 3D sizes that are larger than their cross-sectionally measured sizes, clearly confirming that the stereological effect described above applies in the case of ideal grain growth.

Individual grain behaviors

An essential component of the analytical models of grain growth is a description of the growth kinetics of individual grains [2, 3, 67–69]. However, for the cross sections of 3D microstructures, the behavior of the individual grains has not been investigated to date. Herein, focusing mainly on the cross-sectional grains, we examine the individual grain behaviors and test the applicability of the classical grain growth models.

Hillert [67] proposed a mean-field approximation for both the 3D and 2D grain growth, describing the growth rate of a given grain as a function of its size:
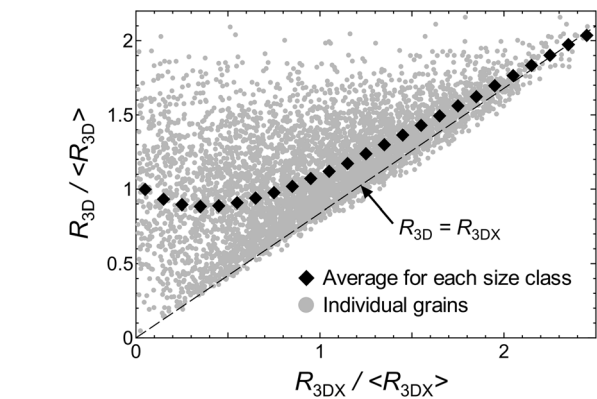

Figure 6 Relationship between cross-sectional and 3D grain sizes at $t = 75000\Delta t_{3D}$. Black diamonds indicate the average 3D grain sizes for each cross-sectional size class obtained by averaging three replicated simulations. The error bars (standard deviations) are all smaller than the symbols. The light-gray circles indicate the data for individual grains, with only 5000 grains randomly sampled from the three simulations plotted to better visualize the density of the data points.

$$R\frac{dR}{dt} = gM\sigma\left(\rho\frac{R}{\langle R\rangle} - 1\right), \tag{10}$$

where g is a geometrical factor that takes a value of 1 for 3D and 0.5 for 2D; ρ is the mean-field parameter given as $\langle R\rangle^2/\langle R^2\rangle$ for 3D and 1 for 2D, where $\langle R^2\rangle$ denotes the average squared grain radius. For fully 2D systems, the von Neumann–Mullins law [68, 69] is well known as a mathematically rigorous formula for individual grain behaviors, which describes the growth rate of a given grain as a function of its topology (number of edges per grain, n_e):

$$R\frac{dR}{dt} = \frac{1}{6}M\sigma(n_e - 6). \tag{11}$$

We tested the applicability of Eqs. (10) and (11) to cross-sectional grain growth by comparing them with the simulated data in the steady-state regime (at $t = 75000\Delta t_{3D}$); the obtained results are given in Figs. 7 and 8, respectively. For comparison, the results for the steady-state 3D and 2D growth are also shown in the figures. Here, since a direct comparison of 3D grain growth behaviors to Eq. (11) is not straightforward, the simulated data for the 3D grains are plotted only in Fig. 7.

As can be seen in Fig. 7a, b, in 3D space there is an almost linear relationship between the growth rate of individual grains and their sizes following the mean-field approximation [Eq. (10)]. Meanwhile, the rate-size relationship in the cross sections of the 3D space is not monotonic, with the growth rate values exhibiting a large

dispersion for grains of the same size. This difference may be attributable to the stereological effect that was discussed above ("Statistical aspects of grain growth" section and Fig. 6), as a result of which the cross-sectional grains appear to have radii that are different from their true 3D values. Since the kinetics of grains in a 3D system are essentially determined by their 3D quantities, the lack of a one-to-one relationship between the 3D and cross-sectional grain sizes can lead to a high degree of randomness in the individual grain behaviors in the cross sections.

In Figs. 7c and 8b, the growth kinetics of the fully 2D grains are observed to conform to both the mean-field approximation [Eq. (10)] and the von Neumann–Mullins law [Eq. (11)]; in particular, as can be confirmed from Fig. 8b, the correlation between the growth rate and grain topology in a 2D system is
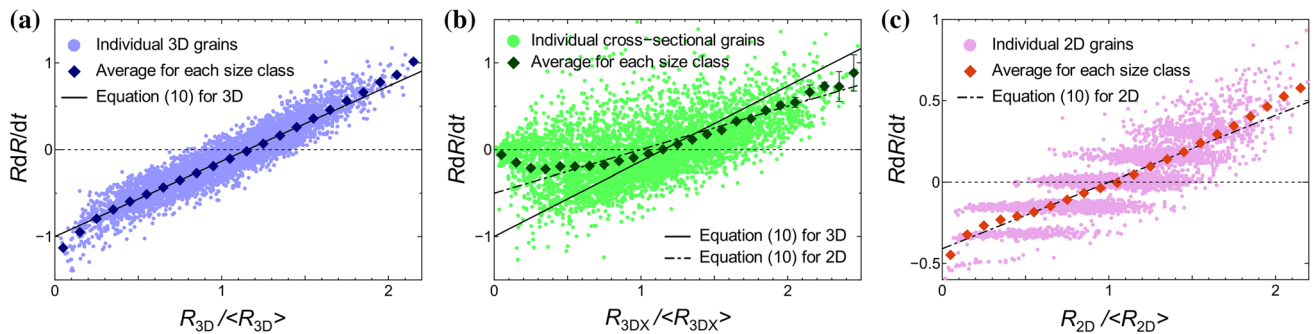

Figure 7 Growth rates of individual grains as functions of their sizes. **a** 3D grains. **b** Their cross sections at $t = 75000\Delta t_{3D}$. **c** 2D grains at $t = 200000\Delta t_{2D}$. The dark-colored diamonds indicate the average for each size class obtained by averaging three replicated simulations, with the error bars representing the standard deviation.

Most of the error bars are smaller than the symbols. The light-colored circles indicate the data for individual grains. To better visualize the density of the data points, only 5000 grains, randomly sampled from the simulations, are plotted in each panel.
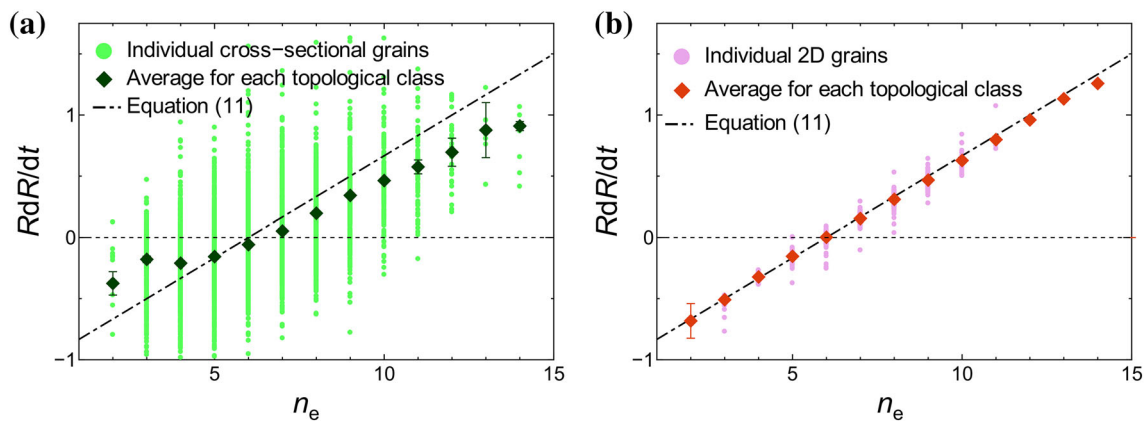

Figure 8 Growth rates of individual grains as functions of their topologies. **a** Cross-sectional grains in 3D system at $t = 75000\Delta t_{3D}$. **b** 2D grains at $t = 200000\Delta t_{2D}$. The dark-colored diamonds indicate the average for each topological class obtained by averaging three replicated simulations, with the error bars

representing the standard deviation. Most of the error bars are smaller than the symbols. The light-colored circles indicate the data for individual grains. To better visualize the density of the data points, only 5000 grains, randomly sampled from the simulations, are plotted in each panel.

quite strong, exhibiting excellent agreement with the von Neumann–Mullins law. A band-like distribution of the data points observed in the RdR/dt versus $R_{2D}/\langle R_{2D}\rangle$ plane (Fig. 7c) can be understood as a consequence of the von Neumann–Mullins law. For instance, most of the grains located along a horizontal line $RdR/dt = 0$ in Fig. 7c belong to the same topological class, $n_e = 6$. In contrast to the case of fully 2D grains, the relationship between the growth rate and topology for cross-sectional grains, shown in Fig. 8a, exhibits a large scatter for those grains belonging to the same topological class. In addition, the curve of the average growth rates for each topological class cannot be described well using the von Neumann–Mullins law. It is clear, therefore, that there is a fundamental difference between full 2D grain growth and the cross-sectional view of 3D growth.

Estimating the 3D grain structure from cross-sectional observations

As demonstrated above, the microstructural characteristics observed in the cross sections are apparently different from those in 3D space due to the stereological effect. In addition, the cross-sectional grain growth cannot be approximated by full 2D growth, in terms of both statistical and individual grain behaviors. Hereafter, based on the simulated results and the stereology, we discuss the estimation of the 3D microstructural characteristics from cross-sectional observations.

First, we focus on the average grain size. From stereological considerations, Fullman [70] showed that if 3D grains are approximated by spheres of a uniform size, the relationship between the 3D average grain size, $\langle R_{3D}\rangle$, and cross-sectional average size, $\langle R_{3DX}\rangle$, can be expressed as:

$$\langle R_{3D}\rangle = \sqrt{\frac{3}{2}}\langle R_{3DX}\rangle \approx 1.225\langle R_{3DX}\rangle. \quad (12)$$

We tested the applicability of this relationship to ideal grain growth by calculating the average size ratio, $\langle R_{3D}\rangle/\langle R_{3DX}\rangle$, using the simulated data shown in Fig. 5a. The results are shown in Fig. 9. We can see that the $\langle R_{3D}\rangle/\langle R_{3DX}\rangle$ value suddenly declines over a short duration. Subsequently, the variation in $\langle R_{3D}\rangle/\langle R_{3DX}\rangle$ occurs very slowly and takes an almost constant value of around 1.2 in the steady state ($t \geq 35000\Delta t_{3D}$), exhibiting good agreement with the estimation given by Eq. (12). Given that the attainment of the steady state in a 3D space can be judged from the cross
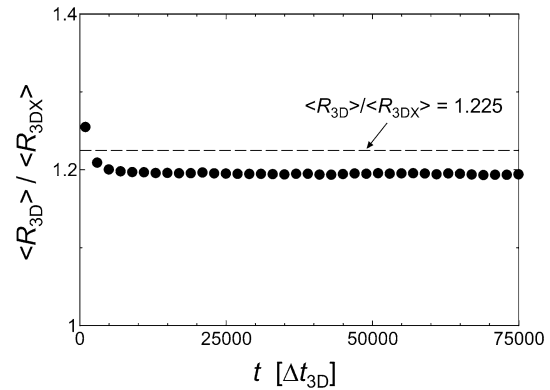

Figure 9 Temporal variations in the ratio of the average grain sizes in 3D and cross sections, as calculated from the data shown in Fig. 5a.

sections (see "Statistical aspects of grain growth" section), we can say that the 3D average grain size can be easily estimated with considerable accuracy based only on cross-sectional observations.

Next, we discuss the prediction of the 3D grain size distribution. In the field of stereology, the Saltykov–Schwartz method [71, 72] is frequently employed to convert cross-sectional and 3D grain size distributions from one to the other [4, 73–76]. Here, we briefly describe this method and propose some modifications. First, let us consider the histograms for 3D and cross-sectional grain size distributions, discretized by m bins. The frequency of the ith size class (within an interval of $R_{3D,i-1}$– $R_{3D,i}$) in 3D is denoted as F_i; that in the cross sections (within $R_{3DX,i-1}$– $R_{3DX,i}$) is denoted as f_i. Considering that a cross section of a given size can arise from 3D grains of various sizes, as demonstrated in Fig. 6, f_i ($i = 1, 2, \ldots, m$) can be expressed by a weighed sum of the series of F_i, that is, as:

$$\begin{cases} f_1 = \alpha_{11}F_1 + \alpha_{12}F_2 + \cdots + \alpha_{1m}F_m, \\ f_2 = \alpha_{21}F_1 + \alpha_{22}F_2 + \cdots + \alpha_{2m}F_m, \\ \quad\quad\quad\quad \vdots \\ f_m = \alpha_{m1}F_1 + \alpha_{m2}F_2 + \cdots + \alpha_{mm}F_m, \end{cases} \quad (13)$$

where α_{ij} is the transformation matrix defined by:

$$\alpha_{ij} = \int_{R_{3DX,i-1}}^{R_{3DX,i}} \int_{R_{3DX,i-1}}^{R_{3DX,i}} c\frac{R_{3D}}{R_{3D,m}} \times p(R_{3D}, R_{3DX}) \, dR_{3D}dR_{3DX}, \quad (14)$$

where $cR_{3D}/R_{3D,m}$ indicates the relative probability of cutting a 3D grain of size R_{3D} by a plane, with c being a normalizing constant determined later; $p(R_{3D}, R_{3DX})$ indicates the probability with which a cross section of size R_{3DX} appears as a result of cutting a 3D grain of

size R_{3D}. Using the α_{ij} matrix, 3D and cross-sectional grain size distribution histograms can be converted to one another:

$$f_i = \alpha_{ij} F_j \quad (i, j = 1, 2, \ldots, m), \tag{15}$$

$$F_j = \alpha_{ij}^{-1} f_i \quad (i, j = 1, 2, \ldots, m). \tag{16}$$

After conversion, the normalizing constant c in Eq. (14) is determined such that the total of the calculated frequencies is equal to 1 (or 100%).

The original Saltykov–Schwartz method models a 3D grain as a sphere. In this case, $p(R_{3D}, R_{3DX})$ in Eq. (14) is rigorously derived, as follows:

$$p(R_{3D}, R_{3DX}) = \frac{R_{3DX}}{R_{3D}\sqrt{R_{3D}^2 - R_{3DX}^2}}. \tag{17}$$

The spherical model gives a relatively simple formula. However, it has been reported that this model is likely to incorrectly estimate the frequency of relatively small grains [77]. Therefore, we propose a modified model which approximates a grain as a Kelvin tetrakaidecahedron, which is well known as a space-filling polyhedron with a minimal surface area and is therefore often employed as a grain model [78–82]. Although a mathematically rigorous expression of $p(R_{3D}, R_{3DX})$ for the tetrakaidecahedron has not yet been established, Matsuura and Itoh [7] evaluated the size distribution of the cross sections of this polyhedron by cutting it with 5000 arbitrary planes via numerical calculations. We depict their results in Fig. 10, comparing them with the analytical curve for a sphere [Eq. (17)], from which we can see that the cutting of the tetrakaidecahedron generates small cross sections with a higher probability than that for a sphere. We created an approximate formula for the tetrakaidecahedron as a weighted sum of the spherical-model function and uniform distribution function:
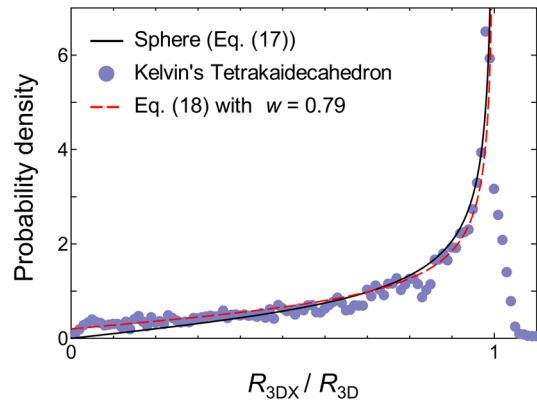

Figure 10 Size distributions of cross sections of 3D objects. The data points for the tetrakaidecahedron indicate the numerical calculation results reported by Matsuura and Itoh [7].

$$p(R_{3D}, R_{3DX}) = w\frac{R_{3DX}}{R_{3D}\sqrt{R_{3D}^2 - R_{3DX}^2}} + (1-w)\frac{1}{R_{3D}}, \tag{18}$$

where w is a weighting parameter, being obtained as $w = 0.79$ by least-square fitting to the data reported by Matsuura and Itoh (Fig. 10).

When a sufficiently large number of grains are sampled, the maxima of the 3D and cross-sectional grain sizes are almost the same value [4]. By setting the maximum sizes in each dimensional grain size histogram to the same value, the transformation matrix α_{ij} [Eq. (14)] with the spherical model [Eq. (17)] can be easily calculated by Cruz-Olive numerical integration [83–85]:

$$\alpha_{ij} = \begin{cases} \dfrac{c}{m}\left\{\sqrt{\left(j-\frac{1}{2}\right)^2 - (i-1)^2} - \sqrt{\left(j-\frac{1}{2}\right)^2 - i^2}\right\} & \text{for } i < j, \\[3mm] \dfrac{c}{m}\sqrt{\left(j-\frac{1}{2}\right)^2 - (i-1)^2} = \dfrac{c}{m}\sqrt{i-\frac{3}{4}} & \text{for } i = j, \\[3mm] 0 & \text{for } i > j. \end{cases} \tag{19}$$

Similarly, with the tetrakaidecahedral model [Eq. (18)] α_{ij} is obtained as:

$$\alpha_{ij} = \begin{cases} \dfrac{c}{m}\left[w\left\{\sqrt{\left(j-\frac{1}{2}\right)^2 - (i-1)^2} - \sqrt{\left(j-\frac{1}{2}\right)^2 - i^2}\right\} + (1-w)\right] & \text{for } i < j, \\[3mm] \dfrac{c}{m}\left\{w\sqrt{i-\frac{3}{4}} + \frac{1}{2}(1-w)\right\} & \text{for } i = j, \\[3mm] 0 & \text{for } i > j. \end{cases} \tag{20}$$

By applying the above stereological method to the simulated data, we tested the possibility of the interconversion of the 3D and cross-sectional grain size distributions in ideal grain growth. Here, the 3D and cross-sectional grain size histograms were built from the simulations during the steady state (at $t = 75000\Delta t_{3D}$) using a typical bin number of 15; the maximum grain size in the histograms was set to $120\Delta x$, which corresponds to the maximum size of cross-sectional grains at the above time. The results are given in Fig. 11. The colored bars show the simulated results as the average of three replicated simulations. The open circles indicate the 3D/cross-sectional size distributions estimated from the cross-sectional/3D simulated data using the spherical-model-based transformation matrix [Eq. (19)]. The filled diamonds denote those using our proposed tetrakaidecahedral-model-based matrix [Eq. (20) with $w = 0.79$]. As shown in Fig. 11, the spherical model incorrectly estimates the frequency of the relatively small grains, especially regarding the prediction of the 3D grain size distribution from the cross sections. In contrast, the tetrakaidecahedral model gives rather smooth curves for both the 3D and cross sections, closely matching the simulated data.

The results presented above allow us to conclude that the average size of the 3D grains in the case of ideal grain growth can be inferred from their cross sections, in line with the classical Fullman theory. Moreover, for the stereological prediction of 3D grain size distribution, although the original Saltykov–Schwartz method based on the spherical grain model exhibits an apparent inaccuracy, its modification using our proposed tetrakaidecahedral model allows for accurately interconverting the 3D and cross-sectional size distributions. Since the average and distribution of 3D grain sizes are dominant factors affecting the physical properties of materials, our findings will be helpful to the application of cross-sectionally observed data to materials design.

Conclusions

The present study was conducted to elucidate the correlations between 3D and cross-sectional microstructures during ideal grain growth. We also attempted to reveal whether the cross-sectional view of 3D grain growth can be modeled by fully 2D grain growth. To this end, 3D and 2D large-scale MPF simulations with approximately three million initial
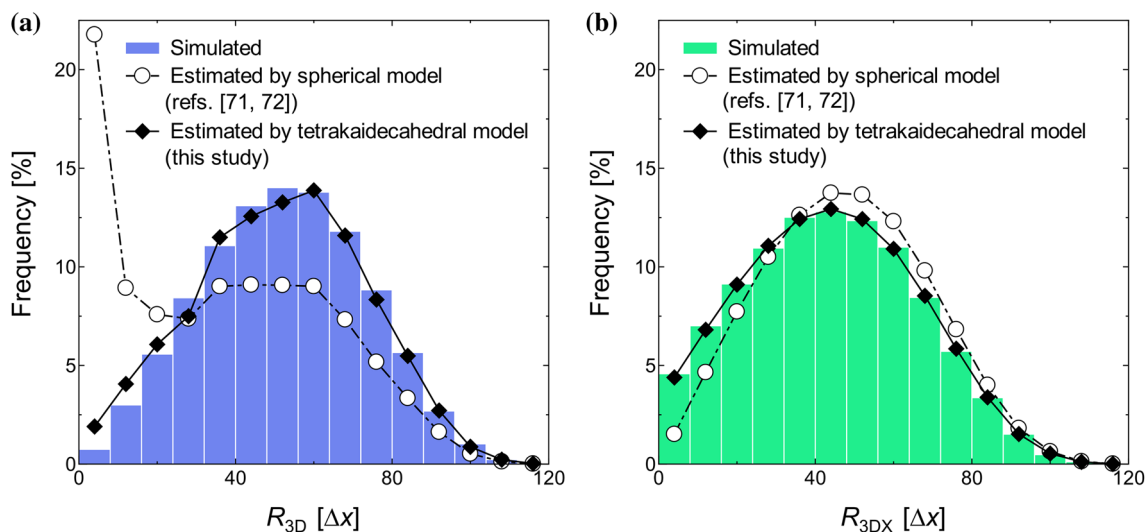

Figure 11 Estimation of **a** 3D and **b** cross-sectional grain size distributions from the measured data in the other dimension. The colored bars show the measured results for the steady-state grain growth (at $t = 75000\Delta t_{3D}$) as the average of three replicated simulations. The open circles indicate the 3D/cross-sectional size distributions, estimated from the cross-sectional/3D measured data using the spherical-model-based transformation matrix [Eq. (19)] that is based on the original Saltykov–Schwartz method [71, 72]; the filled diamonds denote those using the tetrakaidecahedral-model-based matrix [Eq. (20) with $w = 0.79$] proposed in the present study.

grains were performed using multiple GPUs on a supercomputer. This computational scale allowed us to evaluate 3D, cross-sectional, and 2D grain growth with a reasonably high statistical reliability. Based on the simulated results, we discussed how to estimate the microstructural characteristics of 3D grains from those observed in the cross sections. The main findings are summarized as follows:

1. While the steady-state grain size distributions in 3D and 2D show similar symmetrical shapes, that in cross sections exhibits unique characteristics in terms of its right-skewed shape and lower peak height.

2. The temporal variations in the average grain size follow the well-known parabolic law for all of the 3D, cross-sectional, and 2D cases. However, the coefficient of the parabolic law is closely related to the dimensionality.

3. For the 3D and 2D cases, the growth kinetics of individual grains can be described by the mean-field approximation or the von Neumann–Mullins law. In contrast, the individual grain kinetics in the cross sections exhibit a high level of randomness and are not a good match for the above classical grain growth models.

4. The average grain size in the 3D case during steady-state growth can be estimated as being approximately 1.2 times that observed in cross sections, in line with Fullman's stereological prediction.

5. The steady-state 3D and cross-sectional grain size distributions can be interconverted by using our modified Saltykov–Schwartz method that is based on the tetrakaidecahedral grain model.

This study examined the fundamental aspects of cross-sectional grain behaviors by focusing on ideal grain growth. However, it should be emphasized that real materials often contain a considerable amount of structural anisotropy arising from deformation, chemical driving forces, and anisotropic grain boundary properties. This anisotropy may affect the relationship between the microstructural characteristics in 3D and cross sections and could be required to be considered for the practical application of the present stereological predictions. Thus, our future work will study 3D and cross-sectional grain growth in more realistic systems, while quantifying the degree to which they are affected by the anisotropy.

Acknowledgements

Compliance with ethical standards

Conflict of interest The authors declare that they have no conflict of interest.

Electronic supplementary material: The online version of this article (https://doi.org/10.1007/s10853-018-2680-y) contains supplementary material, which is available to authorized users.

References

[1] Humphreys FJ, Hatherly M (2004) Recrystallisation and related annealing phenomena, 2nd edn. Elsevier Ltd., Oxford

[2] Atkinson HV (1988) Overview no. 65. Theories of normal grain growth in pure single phase systems. Acta Metall 36:469–491

[3] Thompson CV (2000) Grain growth and evolution of other cellular structures. Solid State Phys 55:269–314

[4] Russ JC (1986) Practical stereology. Springer, New York

[5] Rhines FN, Patterson BR (1982) Effect of the degree of prior cold work on the grain volume distribution and the rate of grain growth of recrystallized aluminum. Metall Trans A 13:985–993

[6] Hull FC (1988) Plane section and spatial characteristics of equiaxed β-brass grains. Mater Sci Technol 4:778–785

[7] Matsuura K, Itoh Y (1991) Estimation of three-dimensional grain size distribution in polycrystalline material. Mater Trans JIM 32:1042–1047

[8] Rhines FN, Craig KR, DeHoff RT (1974) Mechanism of steady-state grain growth in aluminum. Metall Trans 5:413–425

[9] Liu G, Yu H, Qin X (2002) Three-dimensional grain topology-size relationships in a real metallic polycrystal compared with theoretical models. Mater Sci Eng A 326:276–281

[10] Rowenhorst DJ, Lewis AC, Spanos G (2010) Three-dimensional analysis of grain topology and interface curvature in a β-titanium alloy. Acta Mater 58:5511–5519

[11] Xue W, Wang H, Liu G, Meng L, Ma G, Feng M (2016) Analysis on topological grain forms via large-scale serial sectioning experiment and Monte Carlo simulation. Mater Lett 174:171–174

[12] Döbrich KM, Rau C, Krill CE (2004) Quantitative characterization of the three-dimensional microstructure of polycrystalline Al–Sn using X-ray microtomography. Metall Mater Trans A 35:1953–1961

[13] Bayerlein B, Zaslansky P, Dauphin Y, Rack A, Fratzl P, Zlotnikov I (2014) Self-similar mesostructure evolution of the growing mollusc shell reminiscent of thermodynamically driven grain growth. Nat Mater 13:1102–1107

[14] Cahn RW (1974) Topology of crystal grains. Nature 250:702–703

[15] Doherty RD (1984) Stability of the grain structure in metals. J Mater Educ 6:845–883

[16] Takayama Y, Tozawa T, Kato H, Furushiro N, Hori S (1992) Change in grain size distribution during grain growth. Mater Sci Forum 94–96:325–330

[17] Rowenhorst DJ, Voorhees PW (2012) Measurement of interfacial evolution in three dimensions. Annu Rev Mater Res 42:105–124

[18] Anderson MP, Grest GS, Srolovitz DJ (1989) Computer simulation of normal grain growth in three dimensions. Philos Mag B 59:293–329

[19] Song X, Liu G, Gu N (2000) Re-analysis on grain size distribution during normal grain growth based on Monte Carlo simulation. Scr Mater 43:355–359

[20] Yu Q, Wu Y, Esche SK (2005) Modeling of grain growth characteristics in three-dimensional domains and two-dimensional cross sections. Metall Mater Trans A 36:1661–1666

[21] Kawasaki K, Okuzono T (1990) Computer simulation of cellular pattern growth in two and three dimensions. Phase Transit 28:177–211

[22] Fuchizaki K, Kusaba T, Kawasaki K (1995) Computer modelling of three-dimensional cellular pattern growth. Philos Mag B 71:333–357

[23] Weygand D, Bréchet Y, Lépinoux J, Gust W (1999) Three-dimensional grain growth: a vertex dynamics simulation. Philos Mag B 79:703–716

[24] Mason JK, Lazar EA, MacPherson RD, Srolovitz DJ (2015) Geometric and topological properties of the canonical grain growth microstructure. Phys Rev E 92:063308

[25] Wakai F, Enomoto N, Ogawa H (2000) Three-dimensional microstructural evolution in ideal grain growth—general statistics. Acta Mater 48:1297–1311

[26] Suwa Y (2013) Phase-field simulation of grain growth. Nippon Steel Tech Rep 102:19–24

[27] Kim SG, Kim DI, Kim WT, Park YB (2006) Computer simulations of two-dimensional and three-dimensional ideal grain growth. Phys Rev E 74:061605

[28] Steinbach I, Pezzolla F, Nestler B, Seeßelberg M, Prieler R, Schmitz GJ, Rezende JLL (1996) A phase field concept for multiphase systems. Physica D 94:135–147

[29] Fan D, Chen L-Q (1997) Computer simulation of grain growth using a continuum field model. Acta Mater 45:611–622

[30] Garcke H, Nestler B, Stoth B (1999) A multiphase field concept: numerical simulations of moving phase boundaries and multiple junctions. SIAM J Appl Math 60:295–315

[31] Steinbach I, Pezzolla F (1999) A generalized field method for multiphase transformations using interface fields. Physica D 134:385–393

[32] Kazaryan A, Wang Y, Dregia SA, Patton BR (2001) Grain growth in systems with anisotropic boundary mobility: analytical model and computer simulation. Phys Rev B 63:184102

[33] Moelans N, Blanpain B, Wollants P (2005) A phase field model for the simulation of grain growth in materials containing finely dispersed incoherent second-phase particles. Acta Mater 53:1771–1781

[34] Gruber J, Ma N, Wang Y, Rollett AD, Rohrer GS (2006) Sparse data structure and algorithm for the phase field method. Model Simul Mater Sci Eng 14:1189–1195

[35] Vedantam S, Patnaik BSV (2006) Efficient numerical algorithm for multiphase field simulations. Phys Rev E 73:016703

[36] Suwa Y, Saito Y, Onodera H (2008) Parallel computer simulation of three-dimensional grain growth using the multi-phase-field model. Mater Trans 49:704–709

[37] Darvishi Kamachali R, Steinbach I (2012) 3-D phase-field simulation of grain growth: topological analysis versus mean-field approximations. Acta Mater 60:2719–2728

[38] Vondrous A, Selzer M, Hötzer J, Nestler B (2013) Parallel computing for phase-field models. Int J High Perform Comput Appl 28:61–72

[39] Tegeler M, Shchyglo O, Darvishi Kamachali R, Monas A, Steinbach I, Sutmann G (2017) Parallel multiphase field simulations with OpenPhase. Comput Phys Commun 215:173–187

[40] Yin J, Landau DP (2009) Phase diagram and critical behavior of the square-lattice Ising model with competing

nearest-neighbor and next-nearest-neighbor interactions. Phys Rev E 80:051117

[41] Ohno M (2012) Quantitative phase-field modeling of non-isothermal solidification in dilute multicomponent alloys with arbitrary diffusivities. Phys Rev E 86:051603

[42] Maia JDC, Urquiza Carvalho GA, Mangueira CP, Santana SR, Cabral LAF, Rocha GB (2012) GPU linear algebra libraries and GPGPU programming for accelerating MOPAC semiempirical quantum chemistry calculations. J Chem Theory Comput 8:3072–3081

[43] Knezevic M, Savage DJ (2014) A high-performance computational framework for fast crystal plasticity simulations. Comput Mater Sci 83:101–106

[44] Shibuta Y, Sakane S, Takaki T, Ohno M (2016) Submicrometer-scale molecular dynamics simulation of nucleation and solidification from undercooled melt: linkage between empirical interpretation and atomistic nature. Acta Mater 105:328–337

[45] Shibuta Y, Sakane S, Miyoshi E, Okita S, Takaki T, Ohno M (2017) Heterogeneity in homogeneous nucleation from billion-atom molecular dynamics simulation of solidification of pure metal. Nat Commun 8:10

[46] Shimokawabe T, Takaki T, Endo T, Yamanaka A, Maruyama N, Aoki T, Nukada A, Matsuoka S (2011) Peta-scale phase-field simulation for dendritic solidification on the TSUBAME 2.0 supercomputer. In: Proceedings of 2011 international conference for high performance computing, networking, storage and analysis. ACM, Seattle, pp 1–11

[47] Takaki T, Shimokawabe T, Ohno M, Yamanaka A, Aoki T (2013) Unexpected selection of growing dendrites by very-large-scale phase-field simulation. J Cryst Growth 382:21–25

[48] Shibuta Y, Ohno M, Takaki T (2015) Solidification in a supercomputer: from crystal nuclei to dendrite assemblages. JOM 67:1793–1804

[49] Takaki T, Sakane S, Ohno M, Shibuta Y, Shimokawabe T, Aoki T (2016) Primary arm array during directional solidification of a single-crystal binary alloy: large-scale phase-field study. Acta Mater 118:230–243

[50] Takaki T, Sakane S, Ohno M, Shibuta Y, Shimokawabe T, Aoki T (2016) Large-scale phase-field studies of three-dimensional dendrite competitive growth at the converging grain boundary during directional solidification of a bicrystal binary alloy. ISIJ Int 56:1427–1435

[51] Sakane S, Takaki T, Ohno M, Shibuta Y, Shimokawabe T, Aoki T (2018) Three-dimensional morphologies of inclined equiaxed dendrites growing under forced convection by phase-field-lattice Boltzmann method. J Cryst Growth 483:147–155

[52] Miyoshi E, Takaki T, Ohno M, Shibuta Y, Sakane S, Shimokawabe T, Aoki T (2017) Ultra-large-scale phase-field simulation study of ideal grain growth. npj Comput Mater 3:25

[53] Chockalingam K, Kouznetsova VG, van der Sluis O, Geers MGD (2016) 2D Phase field modeling of sintering of silver nanoparticles. Comput Methods Appl Mech Eng 312:492–508

[54] Suwa Y, Saito Y, Onodera H (2007) Three-dimensional phase field simulation of the effect of anisotropy in grain-boundary mobility on growth kinetics and morphology of grain structure. Comput Mater Sci 40:40–50

[55] Miyoshi E, Takaki T (2017) Multi-phase-field study of the effects of anisotropic grain-boundary properties on polycrystalline grain growth. J Cryst Growth 474:160–165

[56] Backofen R, Barmak K, Elder KE, Voigt A (2014) Capturing the complex physics behind universal grain size distributions in thin metallic films. Acta Mater 64:72–77

[57] Barmak K, Eggeling E, Kinderlehrer D, Sharp R, Ta'Asan S, Rollett AD, Coffey KR (2013) Grain growth and the puzzle of its stagnation in thin films: the curious tale of a tail and an ear. Prog Mater Sci 58:987–1055

[58] Korbuly B, Pusztai T, Henry H, Plapp M, Apel M, Gránásy L (2017) Grain coarsening in two-dimensional phase-field models with an orientation field. Phys Rev E 95:053303

[59] Okita S, Miyoshi E, Sakane S, Takaki T, Ohno M (2018) Grain growth kinetics in submicrometer-scale molecular dynamics simulation. Acta Mater 153:108–116

[60] Miyoshi E, Takaki T, Shibuta Y, Ohno M (2018) Bridging molecular dynamics and phase-field methods for grain growth prediction. Comput Mater Sci 152:118–124

[61] Moldovan D, Wolf D, Phillpot SR, Haslam AJ (2002) Role of grain rotation during grain growth in a columnar microstructure by mesoscale simulation. Acta Mater 50:3397–3414

[62] Vuppuluri A (2018) Theory and simulation of microstructure evolution due to simultaneous grain boundary migration and grain rotation with misorientation dependent energy and mobility. Mater Sci Eng A 713:118–124

[63] Johnson AE, Voorhees PW (2014) A phase-field model for grain growth with trijunction drag. Acta Mater 67:134–144

[64] Moelans N, Wendler F, Nestler B (2009) Comparative study of two phase-field models for grain growth. Comput Mater Sci 46:479–490

[65] Tóth GI, Pusztai T, Gránásy L (2015) Consistent multiphase-field theory for interface driven multidomain dynamics. Phys Rev B 92:184105

[66] Feltham P (1957) Grain growth in metals. Acta Metall 5:97–105

[67] Hillert M (1965) On the theory of normal and abnormal grain growth. Acta Metall 13:227–238

[68] von Neumann J (1952) Discussion—shape of metal grains. In: Herring C (ed) Metal Interfaces. American Society for Metals, Cleveland, pp 108–110

[69] Mullins WW (1956) Two-dimensional motion of idealized grain boundaries. J Appl Phys 27:900–904

[70] Fullman RL (1953) Measurement of particle sizes in opaque bodies. Trans AIME 197:447–452

[71] Saltykov SA (1967) The determination of the size distribution of particles in an opaque material from a measurement of the size distribution of their sections. In: Elias H (ed) Stereology. Springer, New York, pp 163–173

[72] Schwartz HA (1934) The metallographic determination of the size distribution of temper carbon nodules. Met Alloy 5:139–140

[73] Galinari CM, Lameiras FS (1998) Steady-state grain growth in UO2. Scr Mater 39:125–129

[74] Umezaki A, Enomoto M (2000) Estimation of number of precipitate particles per unit volume from measurements on polished specimen surfaces—computer simulation. ISIJ Int 40:1142–1148

[75] Jeppsson J, Mannesson K, Borgenstam A, Ågren J (2011) Inverse Saltykov analysis for particle-size distributions and their time evolution. Acta Mater 59:874–882

[76] Cappia F, Pizzocri D, Schubert A, Van Uffelen P, Paperini G, Pellottiero D, Macián-Juan R, Rondinella VV (2016) Critical assessment of the pore size distribution in the rim region of high burnup UO2 fuels. J Nucl Mater 480:138–149

[77] Mehnert J, Ohser J, Klimanek P (1998) Testing stereological methods for the estimation of spatial size distributions by means of computer-simulated grain structures. Mater Sci Eng A 246:207–212

[78] Hull FC, Houk WJ (1953) Statistical grain structure studies: plane distribution curves of regular polyhedrons. Trans AIME 197:565–572

[79] Cahn JW (1956) The kinetics of grain boundary nucleated reactions. Acta Metall 4:449–459

[80] Umemoto M, Ohtsuka H, Tamura I (1986) Grain size estimation from transformation kinetics. Acta Metall 34:1377–1385

[81] Takayama Y, Furushiro N, Tozawa T, Kato H, Hori S (1991) A significant method for estimation of the grain size of polycrystalline materials. Mater Trans 32:214–221

[82] Chae J, Qin R, Bhadeshia HKDH (2009) Topology of the deformation of a non-uniform grain structure. ISIJ Int 49:115–118

[83] Cruz-Orive LM (1976) Particle size-shape distributions: the general spheroid problem—I. Mathematical model. J Microsc 107:235–253

[84] Cruz-Orive LM (1978) Particle size-shape distributions: the general spheroid problem—II. Stochastic model and practical guide. J Microsc 112:153–167

[85] Pabst W, Treza U (2017) A generalized class of transformation matrices for the reconstruction of sphere size distributions from section circle size distributions. Ceram-Silik 61:147–157